Estimating scatter from sparsely measured primary signal

Gongting Wu,[a,*] Christina R. Inscoe,[a,b] Jabari Calliste,[b] Jing Shan,[c] Yueh Z. Lee,[a,d] Otto Zhou,[a,b,e] and Jianping Lu[a,b]
[a]University of North Carolina at Chapel Hill, Department of Physics and Astronomy, Chapel Hill, United States
[b]University of North Carolina at Chapel Hill, Department of Applied Physical Sciences, Chapel Hill, United States
[c]XinVivo, Morrisville, United States
[d]University of North Carolina at Chapel Hill, Department of Radiology, Chapel Hill, United States
[e]University of North Carolina at Chapel Hill, Lineberger Cancer Center, Chapel Hill, United States

Abstract. Scatter radiation severely degrades the image quality. Measurement-based scatter correction methods sample the scatter signal at sparsely distributed points, from which the scatter profile is estimated and deterministically removed from the projection image. The estimation of the scatter profile is generally done through a spline interpolation and the resulting scatter profile is quite smooth. Consequently, the noise is intact and the signal-to-noise ratio is reduced in the projection image after scatter correction, leading to image artifacts and increased noise in the reconstruction images. We propose a simple and effective method, referred to as filtered scatter-to-primary ratio (*f*-SPR) estimation, to estimate the scatter profile using the sparsely sampled scatter signal. Using the primary sampling device and the stationary digital tomosynthesis systems previously developed in our lab, we evaluated and compared the *f*-SPR method in comparison with existing methods in terms of contrast ratio, signal difference-to-noise ratio, and modulation transfer function. A significant improvement in image quality is observed in both the projection and the reconstruction images using the proposed method.
 [DOI: 10.1117/1.JMI.4.1.013508]

Keywords: measurement-based scatter correction; primary sampling device; CNT x-ray source; scatter estimation; digital tomosynthesis; stationary digital breast tomosynthesis.

Paper 16115PRR received Jun. 19, 2016; accepted for publication Mar. 13, 2017; published online Mar. 29, 2017.

1 Introduction

Scatter radiation is a major issue for x-ray imaging systems using cone-beam x-ray radiation and flat panel detectors. It can severely degrade the image quality by reducing the contrast, increasing image noise, and causing image artifacts, such as the cupping artifact, ring artifact, and streaking artifact.[1,2] Scatter reduction hardware, such as antiscatter grids (ASG), is often used to physically reject the scatter signal. The ASG consists of a series of alternating strips that collimate the radiation and reject scatter coming from directions other than the primary beam. Although scatter radiation is rejected, the primary signal is also reduced due to the collimation, resulting in a decrement of image signal-to-noise ratio (SNR).[3] For digital breast tomosynthesis, the effectiveness of the ASG is still in debate.[4,5] In addition to physically rejecting the scatter signal, mathematical model-based scatter estimation has been intensively investigated. This includes the convolution-based method, Monte Carlo (MC) simulation method, and a hybrid method.[6–10] Among them, the MC simulation method produces the most accurate estimation; however, it requires the most computation time. The convolution-based method estimates scatter by convoluting the projection image with a scatter kernel obtained from MC simulations. The convolution-based method is computationally efficient; however, the scatter estimation is not as accurate. Recent studies showed the computation time of MC simulation could be reduced significantly using advanced graphics processing units (GPUs), making this scatter correction method more practical in the clinical setting.[11–13]

Measurement-based scatter correction method estimates the scatter profile from the sparsely sampled scatter/primary signal.[2,14–18] One method uses a beam-stop (beam-absorber) array (BSA) installed close to the x-ray source.[19–21] The BSA blocks a fraction of the x-ray photons and creates multiple shadow areas on the detector that consist only of scatter. The scatter map is then estimated by interpolating the measured scatter signal under the BSA shadow area. The scatter map estimated using BSA is relatively accurate. However, BSA is prone to residual artifacts due to the missing data.[22] Other techniques, such as the beam-pass array (BPA) and primary modulation method, have also been investigated for sampling and recovering scatter profile.[15,23–25] Previously, our team demonstrated a scatter correction method for stationary digital breast tomosynthesis (s-DBT) using a primary sampling device (PSD).[26,27] Different from BSA/BPA, which are installed close to the x-ray source and have a large magnification factor, the PSD is placed in close proximity to the patient. The magnification for the PSD is close to 1, which allows much smaller size sampling holes and a much higher sampling density than either BPA or BSA, therefore increasing the accuracy of the scatter profile sampling. We have demonstrated that only an additional 3% radiation is needed to obtain a good sampling of the scatter profile, and the method can be easily implemented on digital imaging systems.[26,27]

*Address all correspondence to: Gongting Wu, E-mail: gwu@email.unc.edu

2329-4302/2017/$25.00 © 2017 SPIE

One critical step in the measurement-based scatter correction method is the recovery of the scatter profile from the sparse measurements. The majority of the previous research uses interpolation to generate a smooth scatter profile.[16,17,20,23,28–31] When this scatter profile is subtracted from the projection image, the image noise remains the same. As a result, although the contrast ratio (CR) of the image is increased, the signal difference-to-noise ratio (SDNR) does not change in the projection images. In fact, as shown by Zhu et al.,[32] subtracting a smooth scatter profile will cause noise amplification in the line integral image after logarithmic transformation, resulting in image quality degradation and image artifacts, which may overshadow the benefit of scatter removal.

In this paper, we present a new approach, referred to as the filtered scatter-to-primary ratio (f-SPR) method, to estimate scatter from sparsely sampled scatter signals. Unlike the direct interpolation method, which produces a smooth scatter profile, the f-SPR algorithm scales the high frequency component of the projection image and adds it into the scatter estimation. When the estimated scatter profile is subtracted, the contrast is enhanced and the noise is suppressed, resulting in substantially improved image quality. We quantitatively evaluated the f-SPR method against two direct interpolation methods using breast tomosynthesis data from physical phantoms, and demonstrated its effectiveness using chest tomosynthesis data from a human cadaver imaged by a stationary digital chest tomosynthesis (s-DCT) system.

2 Materials and Methods

2.1 *Scatter Estimation Using Direct Interpolation*

In measurement-based scatter correction, the scatter profile is generally recovered by direct interpolation of the sparse signal samples. There are generally two approaches for scatter estimation. The first approach is to use the measured scatter signal $\bar{S}_i$ at each sampling point i to interpolate the whole scatter profile S_{SI}

$$\begin{aligned}\bar{S}_i &= \text{Average}\,(S)\ \text{within the}\ i\text{'th sampling area}\\ S_{\mathrm{SI}} &= \text{Interpolation}(\bar{S}_i).\end{aligned} \tag{1}$$

We will refer to this method as direct scatter interpolation (SI) in this paper. The scatter profile estimated from the SI method is very smooth, and as a result the noise in the projection image is intact after the scatter subtraction

$$\begin{aligned}\mathrm{Var}(P_{\mathrm{SI}}) &= \mathrm{Var}(T - S_{\mathrm{SI}})\\ &= \mathrm{Var}(T) + \mathrm{Var}(S_{\mathrm{SI}}) + \mathrm{Cov}(T, S_{\mathrm{SI}}) \approx \mathrm{Var}(T),\end{aligned} \tag{2}$$

where P_{SI} stands for the estimated primary signal using SI method and T is the total measured signal. Due to the smoothness of the interpolated scatter profile S_{SI}, $\mathrm{Var}(S_{\mathrm{SI}})$ and $\mathrm{Cov}(T, S_{\mathrm{SI}})$ can be approximated to zero. As a result, the SNR in the SI corrected image is reduced

$$\mathrm{SNR}_{\mathrm{SI}} = \frac{P_{\mathrm{SI}}}{\sqrt{\mathrm{Var}(P_{\mathrm{SI}})}} \approx \frac{P_{\mathrm{SI}}}{\sqrt{\mathrm{Var}(T)}} < \frac{T}{\sqrt{\mathrm{Var}(T)}}. \tag{3}$$

Since neither the signal difference nor the noise variance is changed significantly in the SI corrected images, the SDNR remains the same after scatter correction.

The second approach is to use the measured scatter signal to calculate the scatter-to-primary ratio $\overline{\mathrm{SPR}}_i$ at each sampling point, then interpolating and extrapolating the SPR to the whole image to obtain the SPR profile $\mathrm{SPR}_{\mathrm{intp}}$

$$\begin{aligned}\overline{\mathrm{SPR}}_i &= \text{Average}\,[S/(T-S)]\ \text{at}\ i\text{'th sampling point}\\ \mathrm{SPR}_{\mathrm{intp}} &= \text{Interpolation}(\overline{\mathrm{SPR}}_i),\end{aligned} \tag{4}$$

from which the scatter profile is computed using

$$\mathrm{S}_{\mathrm{ISPR}} = T \cdot \frac{\mathrm{SPR}_{\mathrm{intp}}}{\mathrm{SPR}_{\mathrm{intp}} + 1}. \tag{5}$$

We will refer to this approach as the interpolated SPR (ISPR) estimation. The ISPR method uses a smooth SPR profile to estimate a locally fluctuating scatter signal.[16,30,31,33] ISPR has the advantage of ensuring positivity and enabling further modeling of the scatter profile, for example, one could impose an upper or lower bound threshold on the SPR profile in the ISPR method. At places where scatter varies significantly between two sampling points, ISPR might recover some structural variation of the scatter signal, which SI would fail to estimate. In addition, the ISPR method suppresses the noise in the projection image after scatter removal

$$\begin{aligned}\mathrm{Var}(P_{\mathrm{ISPR}}) &= \mathrm{Var}(T - S_{\mathrm{ISPR}})\\ &= \mathrm{Var}\left[T - T \cdot \left(1 - \frac{1}{\mathrm{SPR}_{\mathrm{intp}} + 1}\right)\right]\\ &= \mathrm{Var}\left[T \cdot \left(\frac{1}{\mathrm{SPR}_{\mathrm{intp}} + 1}\right)\right]\\ &\approx \left(\frac{1}{\mathrm{SPR}_{\mathrm{intp}} + 1}\right)^2 \cdot \mathrm{Var}(T) < \mathrm{Var}(T),\end{aligned} \tag{6}$$

where we approximate $\mathrm{SPR}_{\mathrm{intp}}$ as a constant since the spline interpolation is always smooth between two sampling points. Hence, the SNR will be similar to that in the raw image before scatter correction

$$\begin{aligned}\mathrm{SNR}_{\mathrm{ISPR}} &= \frac{P_{\mathrm{ISPR}}}{\sqrt{\mathrm{Var}(P_{\mathrm{ISPR}})}}\\ &\approx \frac{T \cdot \left(\frac{1}{\mathrm{SPR}_{\mathrm{intp}}+1}\right)}{\sqrt{\left(\frac{1}{\mathrm{SPR}_{\mathrm{intp}}+1}\right)^2 \cdot \mathrm{Var}(T)}} = \frac{T}{\sqrt{\mathrm{Var}(T)}}.\end{aligned} \tag{7}$$

Since the signal difference is also scaled by the same factor, the CR is not enhanced in the scatter corrected image, and the SDNR is not improved.

In summary, scatter correction using scatter profile estimated from direct interpolation of either scatter or SPR samplings would not improve the SDNR of the image.

2.2 *f-SPR Scatter Estimation*

Scatter can be modeled as a convolution of incident x-ray photon flux I and a scatter point spread function SPSF

$$S[r] = \sum_u I[u] \cdot \mathrm{SPSF}(u, r), \tag{8}$$

where $I[u]$ is the total incident photon flux at the image space position u, and the scatter point spread function $\mathrm{SPSF}(u,r)$ describes the scatter kernel from the image space position u to the detector position r. This model suggests that scatter is generally a smooth function on the large scale but could still carry local fluctuations. Direct interpolation of the sparsely measured scatter samplings generates only a smooth scatter profile. The high frequency noise associated with scatter is not subtracted from the image. Though there is no accurate way to estimate this high frequency information, to the first-order it is reasonable to assume that this part of the signal scale with total local signal measured due to the correlation between S and T. And we can make a heuristic approximation

$$\sum_u I[u]\cdot \mathrm{SPSF}(u,r) \approx P[r]\cdot \sum_{r'} \mathrm{SPR}[r']\cdot G(r-r'), \tag{9}$$

where the $G(r-r')$ is a convolution kernel depending only on the distance between two points r and r' in the detector coordinate. The scatter profile, therefore, can be approximated to

$$\begin{aligned} S[r] &\approx P[r]\cdot \sum_{r'} \mathrm{SPR}[r']\cdot G(r-r') \\ &= (T-S)\cdot \mathrm{SPR}_f = T\cdot\left(1-\frac{1}{\mathrm{SPR}_f+1}\right). \end{aligned} \tag{10}$$

For the actual calculation, we use the interpolated scatter profile S_{SI} from the SI method to estimate $\mathrm{SPR}[r']$ using $\mathrm{SPR}_0 = S_{\mathrm{SI}}/(T-S_{\mathrm{SI}})$, and adopt a range bound Gaussian filter kernel as $G(r-r')$

$$\mathrm{SPR}_f = \sum_{r'} \frac{S_{\mathrm{SI}}[r']}{T[r']-S_{\mathrm{SI}}[r']}\cdot G(r-r'). \tag{11}$$

The f-SPR estimated scatter then becomes

$$S_{f-\mathrm{SPR}} = T\cdot\left(\frac{\mathrm{SPR}_f}{\mathrm{SPR}_f+1}\right). \tag{12}$$

Since the filtered SPR profile is a locally smooth function, after the f-SPR scatter correction, noise in the projection image will be suppressed

$$\begin{aligned} \mathrm{Var}(P_{f-\mathrm{SPR}}) &= \mathrm{Var}(T-S_{f-\mathrm{SPR}}) \\ &= \mathrm{Var}\left[T-T\cdot\left(1-\frac{1}{\mathrm{SPR}_{fc}+1}\right)\right] \\ &= \mathrm{Var}\left[T\cdot\left(\frac{1}{\mathrm{SPR}_{fc}+1}\right)\right] \approx \left(\frac{1}{\mathrm{SPR}_{fc}+1}\right)^2\cdot \mathrm{Var}(T), \end{aligned} \tag{13}$$

and the SNR is maintained after scatter correction. Consequentially, SDNR is enhanced after f-SPR scatter correction.

In Eq. (13), we approximate SPR_{fc} as a constant. This approximation holds when the filtered SPR profile is locally smooth. However, if the filter size is close to zero, this approximation fails and the noise variance of the f-SPR corrected image converges to that of the SI corrected image. As will be later demonstrated, the filter size controls the amount of the total signal that is scaled and copied to the scatter estimation. When the filter size is zero, f-SPR is essentially the SI method; when the filter size increases to the range of the sampling distance, f-SPR converges to ISPR. Unlike the ISPR where the true signal is scaled, the signal difference would not be scaled much at the small filter size in f-SPR. In f-SPR, as shown in Eq. (12), the smooth SI scatter profile is adapted to compute SPR before filtering, and this sets the baseline of the scatter estimation and prevents the true signal from being copied into the scatter estimation. In essence, the f-SPR method combines the advantage of the SI method, which enhances the contrast and the ISPR method, which reduces the noise to result in an enhanced SDNR. A flow chart of the f-SPR method is shown in Fig. 1.

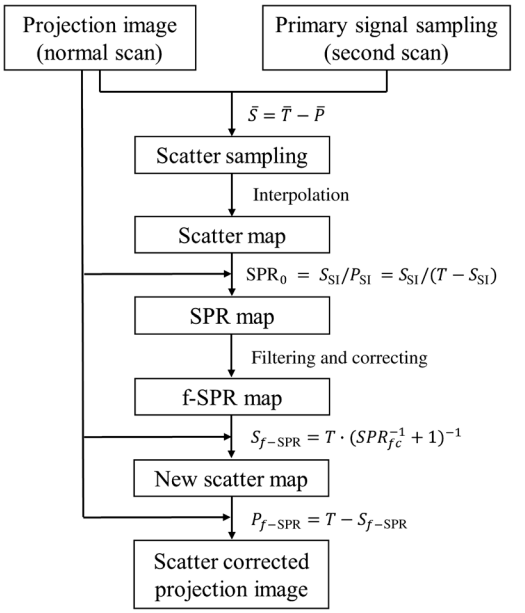

Fig. 1 Flow chart of the f-SPR scatter estimation method.

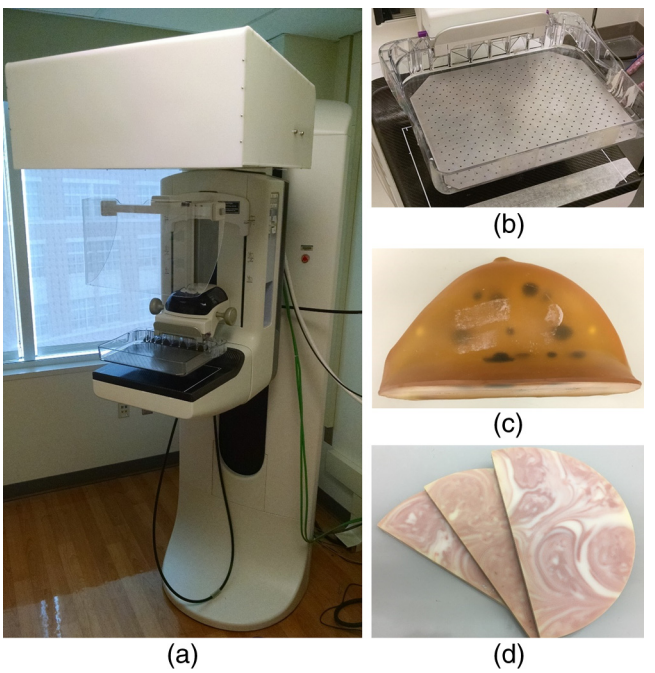

Fig. 2 (a) s-DBT system with PSD installed. (b) The PSD designed for the s-DBT system is placed on the compression paddle. (c) Breast biopsy phantom. (d) BR3D breast imaging phantom.

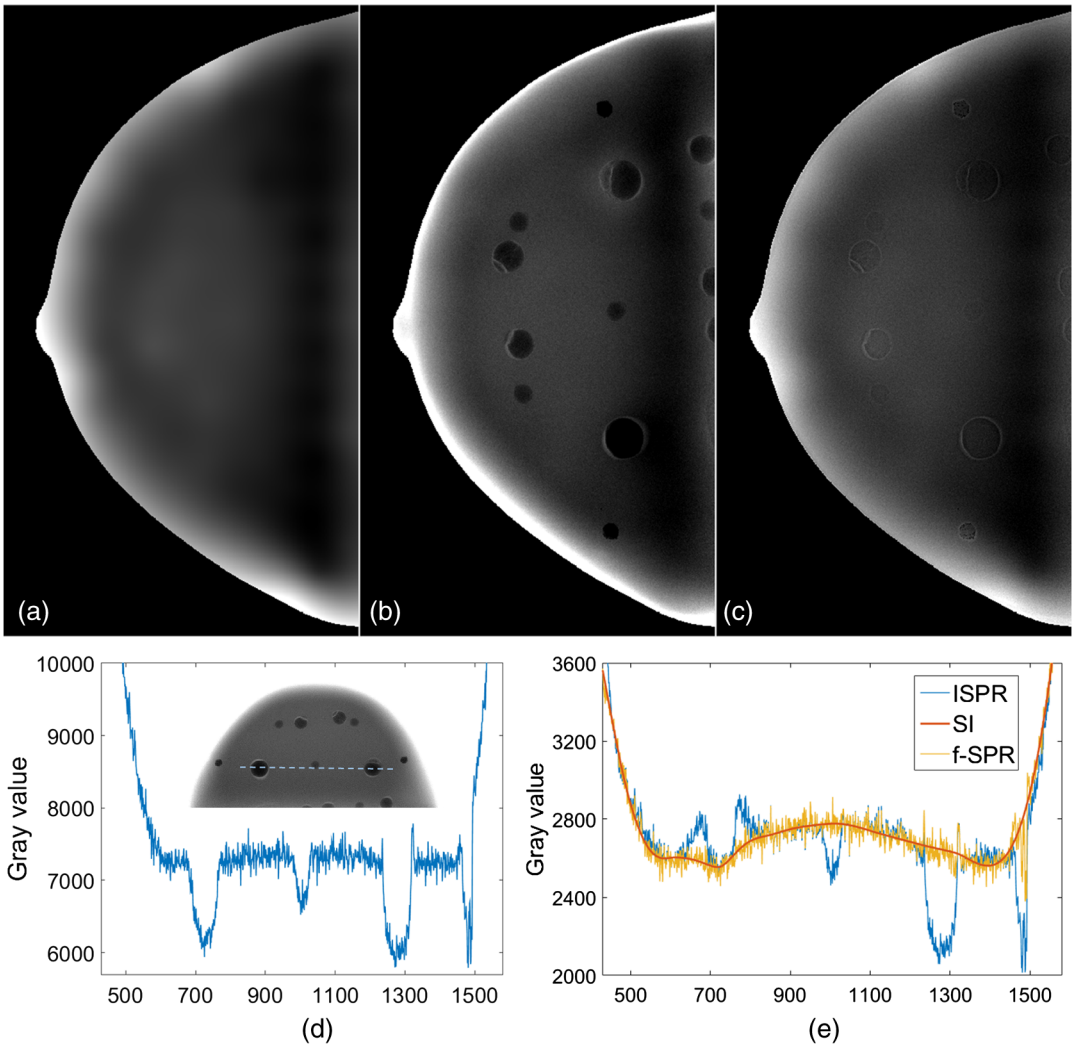

Fig. 3 Scatter profile of the central projection view estimated by (a) SI, (b) ISPR, and (c) *f*-SPR method. The scatter signal outside the phantom is set to be zero to avoid artifact during reconstruction. All scatter profiles are shown at the same display window. (d) Line profile of the projection image before scatter correction. The position is indicated by the blue dashed line on the biopsy phantom. (e) Profiles of scatter estimated by different methods along the same line. The SI estimated scatter is very smooth and does not contain any noise. The ISPR estimated scatter though over/underestimates the scatter in the region with object features. The *f*-SPR estimation captures both the large-scale smooth variation and the local fluctuation of the scatter profile.

The first step in f-SPR is segmenting out the sampling region in the scan with PSD installed. This is done using Otsu's threshold method with a morphological closing operation.[34] To avoid the penumbral effect, the identified sampling area is morphologically eroded by 4 pixels. Next, the center of each sampling area is located and the average scatter signal of each sampling area is computed using $\bar{S} = \bar{T} - \bar{P}$, where $\bar{P}$ is the average primary signal measured from the PSD scan and $\bar{T}$ is the average total signal measured from the normal scan in the same sampling region. A biharmonic spline interpolation and extrapolation is then applied on the sparse scatter samplings and the SI estimated scatter profile S_{SI} is obtained.[35] Based on this smooth scatter profile S_{SI}, the SPR at each pixel is calculated using $\mathrm{SPR} = S_{\mathrm{SI}}/(T - S_{\mathrm{SI}})$.

At regions with structural change, such as places with metal implants, the scatter signal might be overestimated since the finite sampling points might be too sparse to capture the change. To avoid overestimation, the computed SPR profile is corrected using a preset maximum SPR value obtained from previous studies.[36,37] This structural variation of the scatter signal could also be recovered using the information from the adjacent scatter profile through mathematical modeling.[22] In this study, we set a maximum SPR value of 2 for breast imaging and a maximum SPR value of 10 for thoracic imaging. After correction, the SPR profile is convoluted with a Gaussian filter kernel and the filtered SPR profile is obtained [Eq. (12)]. In this study, we used a Gaussian filter with standard deviation σ of 4 pixels and filter size equal to 17 pixels (see Sec. 4 on the choice of filter size). Finally, the scatter-corrected projection image is obtained: $P_{f-\mathrm{SPR}} = T - S_{f-\mathrm{SPR}} = T \cdot \left(\frac{1}{\mathrm{SPR}_{fc}+1}\right)$.

2.3 *Imaging System*

2.3.1 *Stationary digital breast tomosynthesis*

An s-DBT system was used for breast imaging studies.[38,39] The s-DBT system uses field emission-based carbon nanotube x-ray

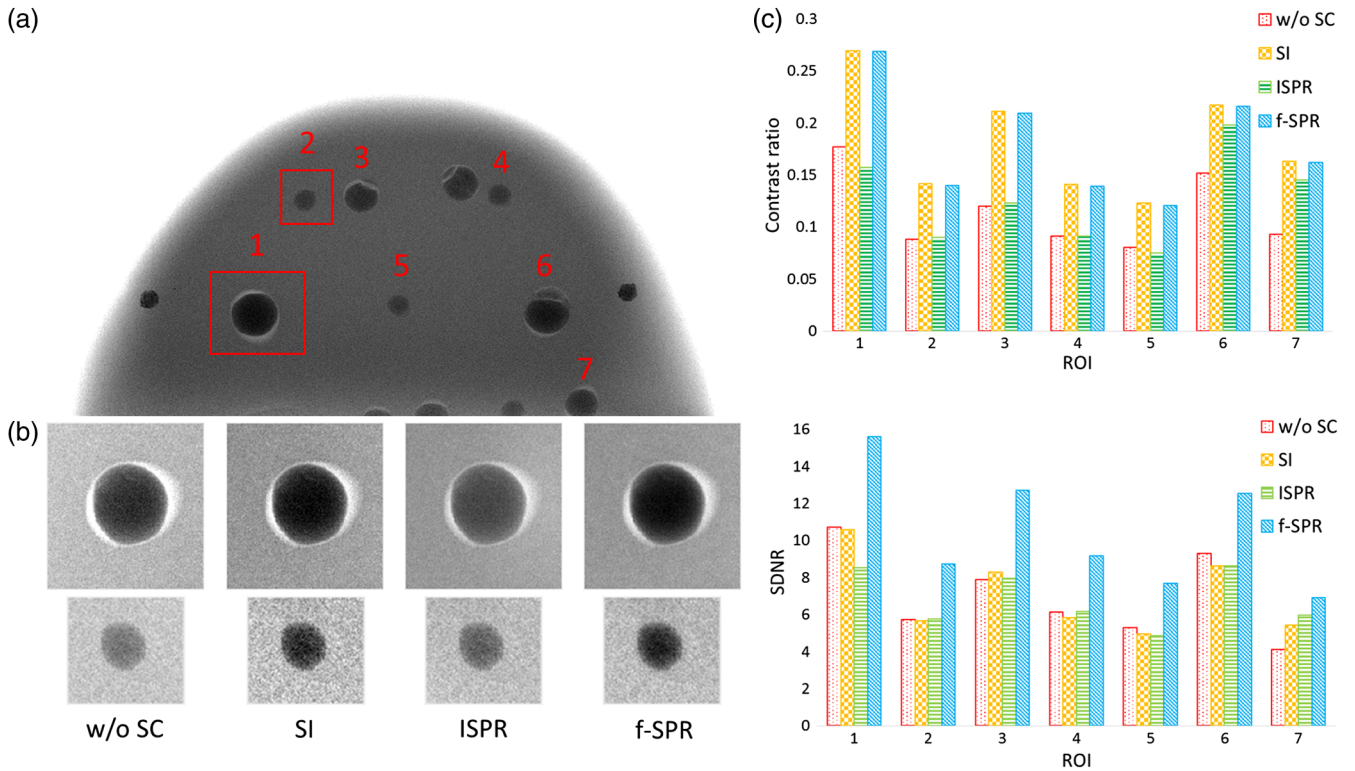

Fig. 4 (a) Central projection view of the breast biopsy phantom. The display window is set for visualization of the internal structure. The index marks seven regions that are used in CR and SDNR analysis. (b) Enlarged view of region 1 and region 2 (from left-to-right: without scatter correction, SI corrected, ISPR corrected, and *f*-SPR corrected images). (c) The CR and SDNR for the seven ROIs. Both SI and *f*-SPR corrected images show a significant improvement in CR, but only *f*-SPR shows significant enhancement in SNDR. On average, a 58% increase in CR and 51% increase in SDNR are observed with *f*-SPR scatter correction method.

source array, which eliminates the mechanical source motion in the traditional tomosynthesis scan. The s-DBT system has a linear x-ray source array with 31 focal spots and an angular coverage of 28 deg, a typical anode voltage of 31 kVp, a detector pixel size of 70 μm, and an image resolution of 3328×4096.[39] In this study, we used only 15 projection images with 28 deg angular coverage in 2×2 binning mode, with an equivalent pixel size of 140 μm. Figure 2(a) shows the s-DBT system, which is undergoing clinical trials at the University of North Carolina Hospital (NCT01773850, NCT02008032).

2.3.2 *Stationary digital chest tomosynthesis*

The s-DCT system employees similar x-ray source array technology. It uses a linear source array with 75 focal spots and an angular coverage of 15 deg at 100 cm source-to-detector distance, and the anode voltage is 80 kVp. A flat panel detector is used in the s-DCT system, which has 1536×1536 pixels and a pixel size of 194 μm.[38] The s-DCT system is also currently under a clinical trial at the Biomedical Research Imaging Center at the University of North Carolina (NCT02075320).

2.4 *Primary Sampling Device*

The PSD is a thin metal plate with an array of small open apertures.[26,27] As x-ray photons can penetrate only through the open apertures, the projection of the apertures on the detector contains mostly the primary signals, and the primary photons in each projection view can therefore be sampled using PSD.

During the scatter correction, normal projection images are first acquired without PSD. After the normal scan, a second scan is performed with the PSD installed close to the imaged object. By comparing the total signal intensity from the normal scan and the primary signal intensity from the second scan, samplings of scatter/SPR are obtained, which are used to estimate the full scatter map.

The PSD used with the s-DBT system is made of a 2-mm-thick stainless steel plate, containing apertures of 2 mm diameter with 10.6 mm spacing. This translates to an aperture area of only 3% of the total area, resulting in a minimal additional dose.[26] Figures 2(a) and 2(b) show a PSD placed on the compression paddle of the s-DBT system. The PSD used in the s-DCT system is made of a 6-mm-thick lead plate, containing apertures spaced 31 mm apart with a diameter of 6 mm, also occupying about 3% of the total plate area.[27]

2.5 *Phantom Studies*

A breast biopsy phantom and BR3D breast imaging phantom (Computerized Imaging Reference Systems, Virginia) are used in this study to demonstrate and evaluate the *f*-SPR method. Both phantoms were imaged by the s-DBT system. Pictures of the biopsy phantom and the BR3D phantom are shown in Figs. 2(c) and 2(d), respectively. In this study, we used three BR3D slabs, one feature slab with mass and microcalcification simulants sandwiched between two breast tissue mimicking slabs. The thickness of each slab is 1 cm. A 50-μm-diameter tungsten wire phantom placed on top of three BR3D

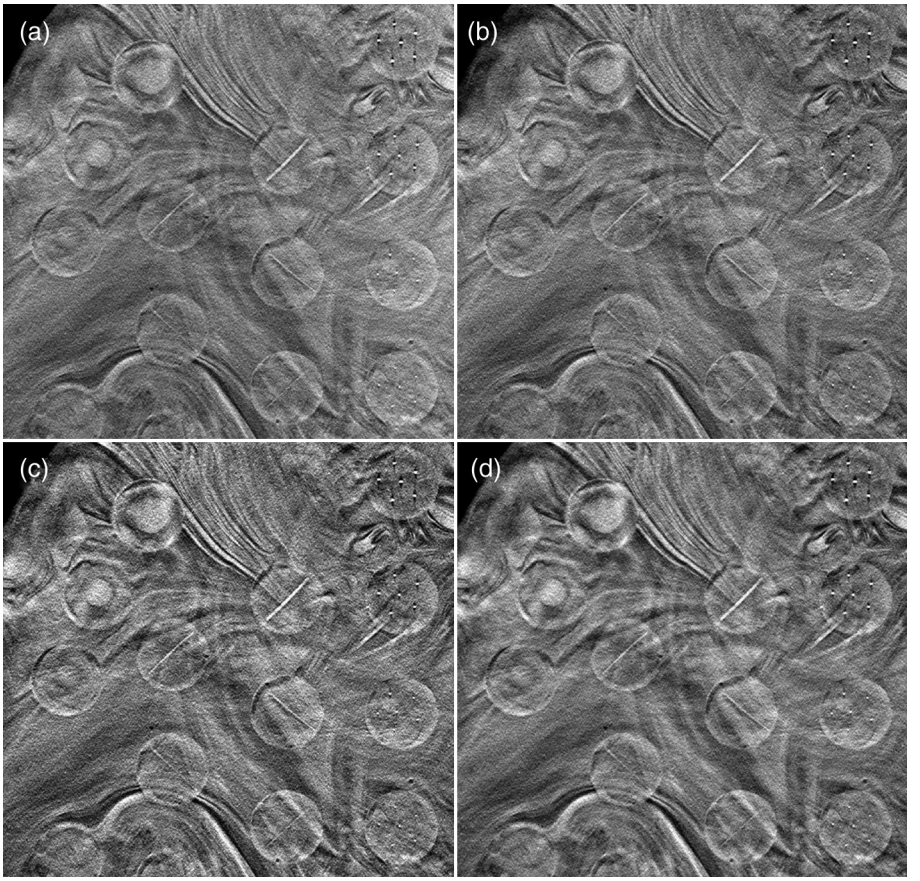

Fig. 5 In-focus reconstruction slice of the BR3D feature slab: (a) without scatter correction, (b) with ISPR, (c) with SI, and (d) with *f*-SPR scatter correction. All images are displayed at the same window width. The window level is set to be the average of the image intensity. Reconstruction with *f*-SPR correction has a significantly better SDNR compared to reconstruction with other scatter correction methods, and a CR comparable to that in the reconstruction with SI correction.

adipose slabs is used to measure the system's modulation transfer function (MTF).

An adult female thoracic cadaver, obtained through collaboration with the UNC School of Medicine, was imaged by the s-DCT system. The thickness of the thorax is 25 cm.

2.6 *Image Reconstruction*

Scatter-corrected projection images are reconstructed using the adapted fan volume reconstruction (AFVR) method.[40] AFVR utilizes the linear source geometry in the stationary tomosynthesis, in which it transforms the three-dimensional cone-beam reconstruction into a series of two-dimensional (2-D) fan volume reconstructions. In AFVR, each 2-D fan volume reconstruction is independent and its system matrix is precalculated and stored in memory. This makes AFVR extremely fast, even without the GPU implementation. In this study, a simultaneous iterative reconstruction technique with 20 iterations was used.[41] The reconstructed slice thickness is 0.5 mm for the biopsy and BR3D phantom, and 3 mm for the human cadaver.

2.7 *Evaluation Metrics*

The effectiveness of the f-SPR method is evaluated using the CR and SDNR. CR is calculated using $\mathrm{CR} = (I_f - I_b)/I_b$, where I_f is the average pixel value of the foreground (features), and I_b is the average pixel value of the background area around the features.

Practically, the local CR is usually stretched and maximized by adjusting the image display window. A more meaningful metric for measuring the image quality is the ability to differentiate structures/tissues, given the presence of the background noise. This is measured using the SDNR, defined as: $\mathrm{SDNR} = (I_f - I_b)/\sigma_b$, where σ_b is the noise level of the background.

The spatial resolution is characterized by the MTF. A 50-μm slanted tungsten wire phantom was used to measure the system MTF. SI, ISPR, and f-SPR methods were applied to the projection images, and the scatter corrected projection images were then reconstructed using AFVR. Finally, using the slice containing the focused wire, the MTF was obtained using the method described by Fujita et al.[42]

3 Results

3.1 *Scatter Correction on Projection Image*

Figures 3(a)–3(c) show the scatter profiles estimated using different methods for the breast biopsy phantom in the central projection view. The SI estimated scatter is very smooth since it is obtained directly from interpolation; the ISPR estimated scatter, on the other hand, is quite noisy and it even shows features from the projection image. The f-SPR estimated scatter looks quite similar to the SI estimated scatter except that it is locally grainy,

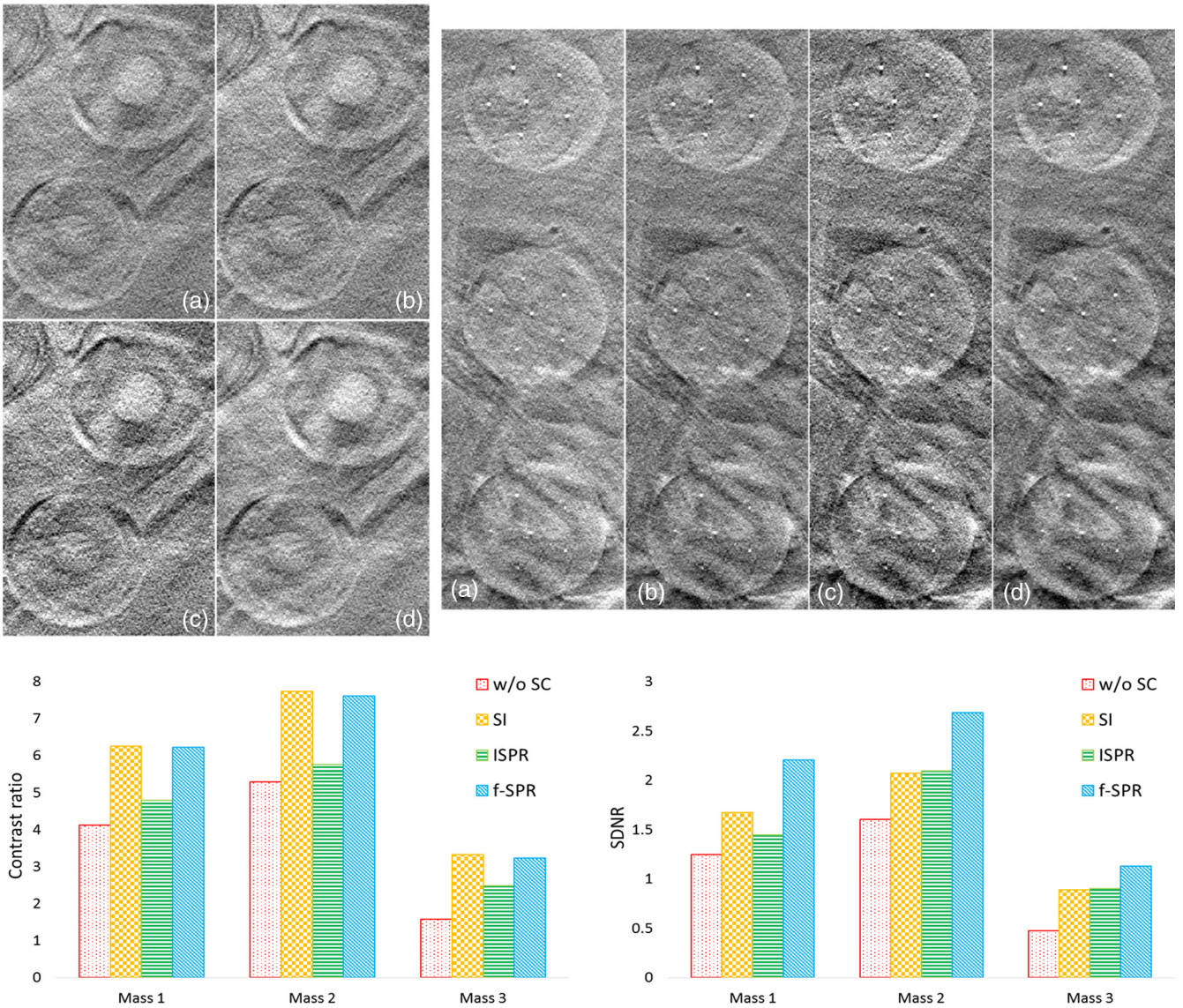

Fig. 6 Top left: in-focus reconstruction slice of two spheroid masses in the BR3D phantom (a) without scatter correction, (b) with ISPR, (c) with SI, and (d) with *f*-SPR scatter correction. Top right: in-focus reconstruction slice of microcalcifications in the BR3D phantom (a) without scatter correction, (b) with ISPR, (c) with SI, and (d) with *f*-SPR scatter correction. All images are displayed at the same window width. Bottom: CR and SDNR of three spheroid masses. Both CR and SDNR are improved after scatter correction, and the *f*-SPR method is clearly superior to the SI and ISPR methods. On average, a 66% increment in CR and 94% increment in SDNR are observed on the *f*-SPR scatter corrected reconstruction.

since the high frequency spectra of the total signal is scaled and added into the scatter estimation. The characteristics of three estimated scatter profiles are better illustrated from the line profiles shown in Fig. 3(e). In ISPR, the SPR map used to estimate scatter is smooth due to direct interpolation. Although the ISPR method has better noise properties, the signal difference is decreased in comparison to the projection image without scatter correction. The SI method estimates a very smooth scatter profile and the noise in the original projection image is unaffected by the scatter correction. Therefore, the scatter-corrected image is quite noisy using the SI method. The f-SPR estimated scatter is smooth on a large scale but fluctuates locally. The scatter-corrected image using f-SPR maintains the signal difference, as in the SI corrected image, but suppresses the noise during the scatter correction. It results in an improved SDNR in the projection image, which consequently leads to a better reconstruction image.

To quantitatively evaluate the projection image quality after scatter correction, we selected seven regions of interest (ROI) across the phantom and computed both CR and SDNR for each ROI. Figure 4 shows the locations of each ROI [Fig. 4(a)], enlarged views of the central projection images after applying different scatter correction methods, [Fig. 4(b)] and CR and SDNR of the seven regions. [Fig. 4(c)] As seen in the figure, both the SI and f-SPR corrected images show a significant improvement in the CR; however, only the f-SPR corrected projection image shows an improved SDNR. In the ISPR corrected image, the CR and SDNR are comparable or only slightly better than the projection image without scatter correction. Overall, we observed an average of 58% increment in CR and an average

of 51% increment in SDNR in the projection image corrected using f-SPR method.

3.2 *Reconstruction Image Quality Analysis*

The in-focus reconstruction slices of the BR3D phantom before and after scatter correction are shown in Fig. 5. Compared to the reconstruction image without scatter correction, all scatter-corrected reconstruction images show higher contrast and better conspicuity. Both SI and f-SPR corrected reconstruction slices show a noticeably improved contrast; however, the noise is significantly lower in the f-SPR corrected image. ISPR corrected reconstruction slice shows a low noise level; however, the improvement of the image contrast is not as good as that in the reconstruction corrected using SI or f-SPR.

Enlarged views of spheroid masses and microcalcifications are shown in Fig. 6. Both SI and f-SPR corrected reconstructions show significant improvement in contrast; however, the pronounced noise in the SI corrected image makes it difficult to identify small features such as microcalcifications from the image. On the other hand, f-SPR corrected reconstruction has a noise level similar to that in the uncorrected and the ISPR corrected reconstructions, but with a much higher CR, making it easy to identify both masses and microcalcifications on the image.

Quantitative analysis of CR and SDNR on three spheroid masses is shown in Fig. 6. Three largest masses in the BR3D phantom were chosen for this analysis with diameters of 6.3, 4.7, and 3.9 mm. For masses, the results show the CR is improved by 69.5%, 27.4%, and 66.5% for SI, ISPR, and f-SPR corrected reconstruction, respectively. The SDNR is improved by 49.8%, 45.1%, and 93.8% for SI, ISPR, and f-SPR corrected reconstruction, respectively. The results suggest that the f-SPR corrected reconstruction has a comparable increment in the CR, and almost doubles the increment in SDNR compared to SI corrected reconstruction. The ISPR corrected reconstruction has improvement in both CR and SDNR; however, the increment is not as good as that in either SI corrected or f-SPR corrected reconstruction.

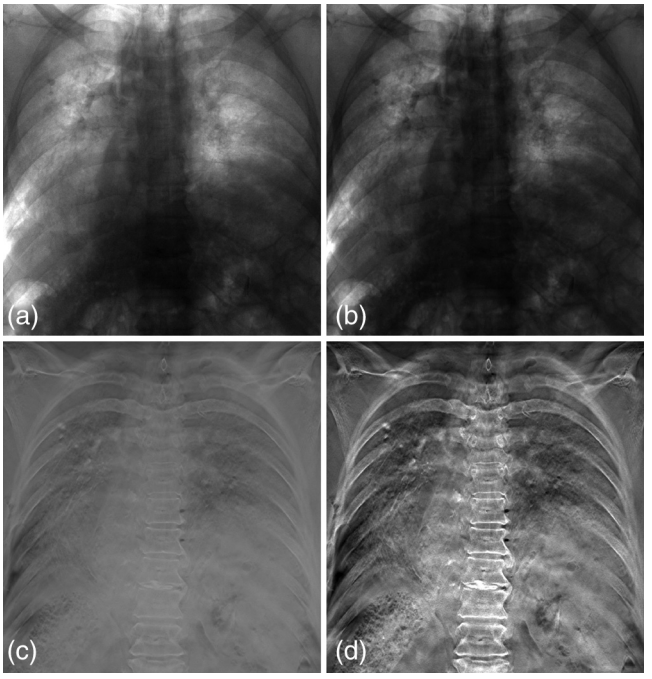

Fig. 7 Human cadaver imaged by s-DCT. Projection image of the central view (a) without scatter correction, (b) with f-SPR scatter correction. Reconstruction image (c) without scatter correction and (d) with scatter correction. Images before and after f-SPR scatter correction are displayed at the same window width, but different window level, which is set to be the mean gray value of the image. The f-SPR scatter correction improves the conspicuity in both projection and reconstruction images.

3.3 *Chest Imaging*

We further implemented PSD with the f-SPR correction on an s-DCT system for chest imaging. A human cadaver was imaged using s-DCT with an additional PSD scan. The f-SPR scatter correction was then applied on the projection images, which were later reconstructed using AFVR. Both projection views and reconstruction images with and without f-SPR scatter correction are shown in Fig. 7. The f-SPR scatter correction improves image contrast in both projection and reconstruction images. Body anatomy and fine features become more conspicuous after scatter correction.

4 Discussion

4.1 *Filter Size in f-SPR Scatter Correction*

One of the most important steps in f-SPR is the filtering. Using Pearson's correlation,[43] we investigated the similarity between the f-SPR estimated scatter and direct interpolation estimated scatter when varying filter size. The standard deviation of the Gaussian filter σ is set to be $0.25 \cdot (\text{filter size} - 1)$, and the central region is used for computing Pearson's correlation. The result is shown in Fig. 8. When no filtering is applied on the SPR map, the f-SPR is equivalent to SI and the Pearson's correlation is one. As the filter size increases, the Pearson's correlation between SI and f-SPR estimated scatter decreases. On the other hand, the correlation between f-SPR and ISPR estimated scatter increases as the filter size increases. When the size of filter reaches the distance between two sampling points, the correlation between f-SPR estimated scatter and ISPR estimated scatter is close to one.

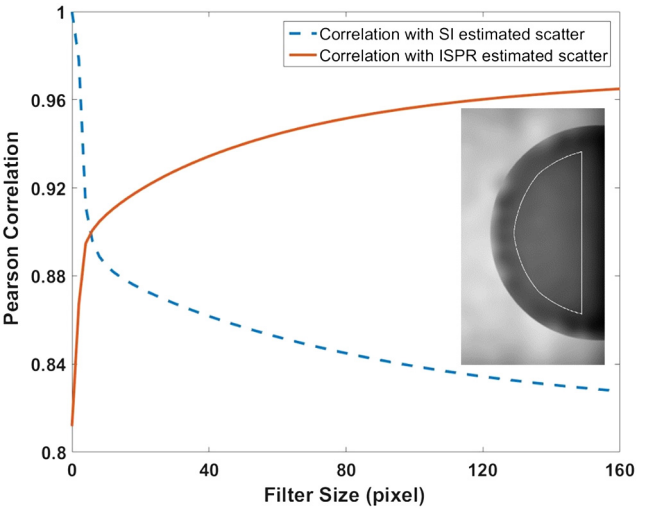

Fig. 8 Correlation of scatter profile between the f-SPR estimation and the SI/ISPR estimation. The white line on the scatter map indicates the area that is used to compute the correlation.

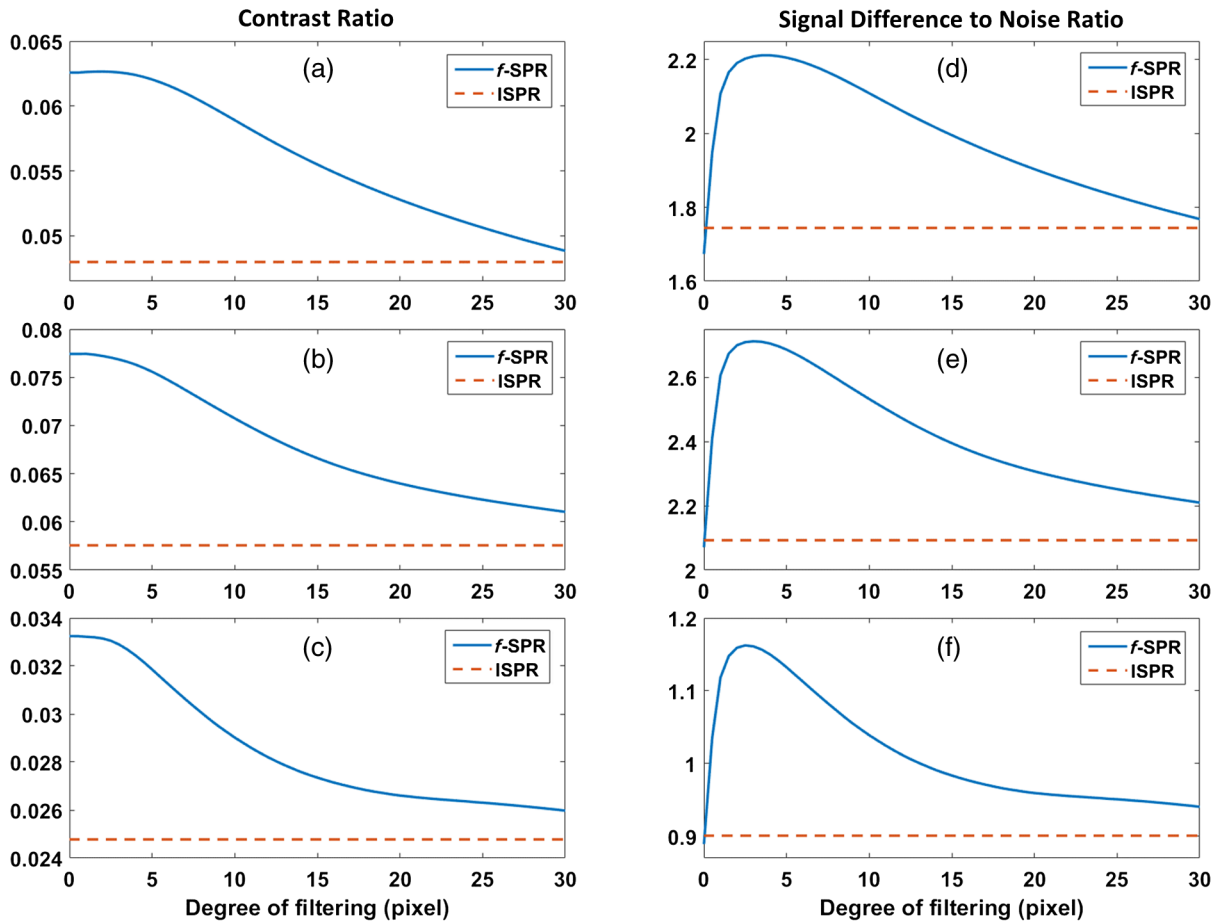

Fig. 9 CR of (a) mass 1, (b) mass 2, and (c) mass 3. SDNR of (d) mass 1, (e) mass 2, and (f) mass 3. The solid blue line depicts the *f*-SPR scatter-corrected reconstruction, while the red dashed line depicts the ISPR scatter-corrected reconstruction. The CR and SDNR in the SI scatter-corrected reconstruction are the same as those of the *f*-SPR with no filtering. The *x* axis is the standard deviation of the Gaussian filter.

The image quality, in terms of CR and SDNR, is also studied with varying filter sizes. The three largest spherical masses in the feature slab were chosen for this analysis, with results shown in Fig. 9. The results suggest that when the filter size is small, the image quality of the f-SPR corrected reconstruction is similar to that of the SI corrected reconstruction; when the filter size is large, the image quality of f-SPR corrected reconstruction is more similar to the ISPR corrected reconstruction. The SDNR curve increases and then decreases, with a peak value around 4 pixels. The increase in SDNR when the filter size is small is probably due to the plateau region in the CR curve, where CR is maintained as the noise decreases with filter size. As the filter size further increases, the CR starts to drop but the noise level is not further reduced. Hence, the SDNR drops and finally matches the SDNR in the ISPR corrected reconstruction image.

4.2 *Image Resolution with f-SPR Scatter Correction*

One concern about the f-SPR algorithm is the possible loss of the spatial resolution due to the filtering. Visual inspection of the small features, such as microcalcification, shows no image blur on the f-SPR corrected reconstruction image. To quantitatively investigate the possible image resolution change, we measured the system MTF before and after scatter correction, and the result is shown in Fig. 10. The image resolution at 10% MTF before scatter correction is 4.5 line/mm, and it drops slightly to 4.4 line/mm after f-SPR scatter correction using a Gaussian filter with a filter size of 17×17 pixel. Both the SI corrected and ISPR corrected reconstruction show similar frequency at 10% MTF. However, the reconstruction from Gaussian filtered SI corrected projection data using the same filter as f-SPR shows severe degradation in the image resolution, with the 10% MTF at 0.8 line/mm. The MTF curves are consistent with our visual observation.

4.3 *Advantages, Limitations, and Future Work*

One advantage of using SPR for scatter correction is that the noise in the projection image is suppressed after the scatter removal. An underlying assumption of this approach is that the noise in the scatter signal and the noise in the total signal are correlated. This is a valid assumption considering that a large portion of the total signal is scatter, especially in the regions with high SPR values. This assumption could be inaccurate in the regions with very low scatter; however, the high frequency correction that will be applied at those regions is also small.

Scatter correction using SI improves the local CR but it fails to reduce noise, while correction using ISPR reduces the noise level but it fails to improve the local contrast. The f-SPR method takes the advantages of both scatter estimations and balances between the two with different levels of filtering. When no

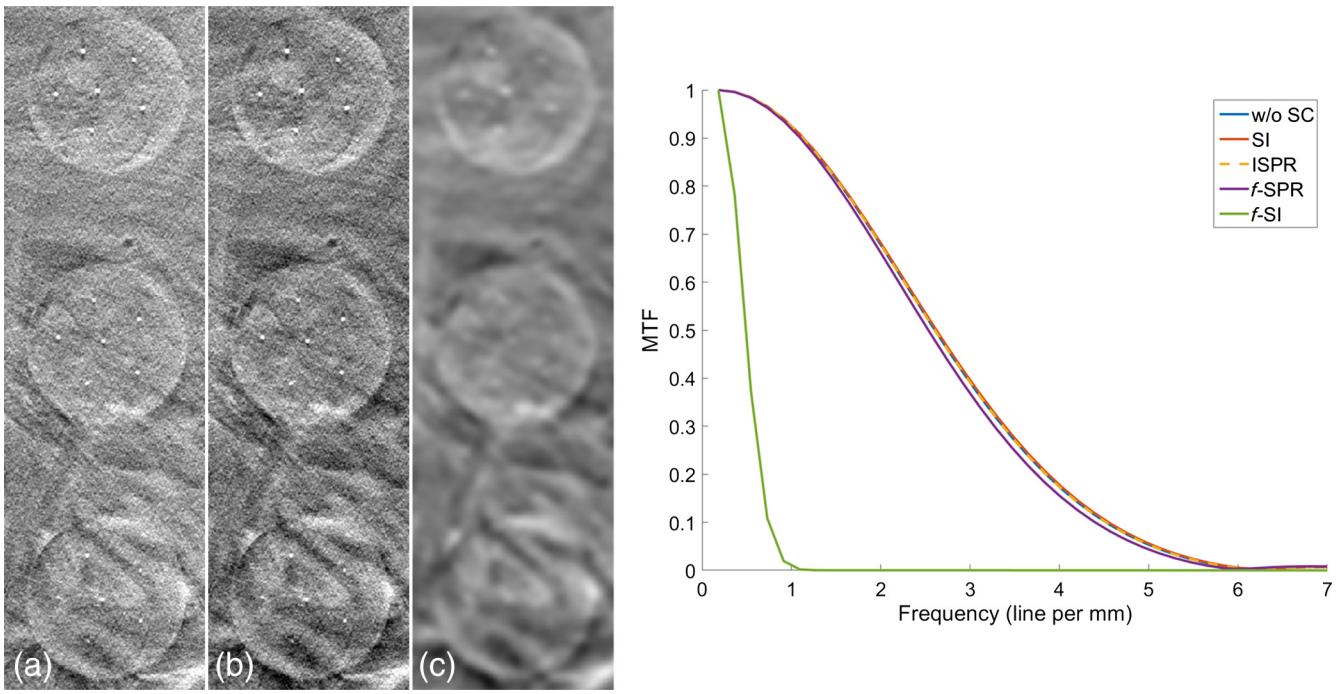

Fig. 10 Left: enlarged view of microcalcifications in the in-focus reconstruction slice of the BR3D phantom: (a) without scatter correction, (b) with *f*-SPR scatter correction, and (c) with direct Gaussian filtering on the SI corrected projection data (*f*-SI). Right: system MTF curve using different processing methods. It is clear that the *f*-SPR method has negligible impact on the spatial resolution, while direct filtration of the SI corrected image with the same filter size dramatically reduces the spatial resolution.

filtering is applied, the f-SPR is the same as the SI scatter correction. When the scale of filtering is close to the PSD sampling distance, the scatter estimated by f-SPR and ISPR becomes quite similar to each other.

In this paper, we analyzed the image quality of different scatter correction methods, and showed that the noise is reduced and the SDNR is increased on the projection images using the proposed f-SPR method. Due to the nonlinear characteristics of the logarithmic transformation, the noise property would be different on the line integral images.[32] The improvement of image quality, however, is still valid after the logarithmic transformation, since better projection images will lead to better line integral images, which eventually leads to better reconstruction images.

The effect of off-focal radiation has been investigated in a separate study using the s-DBT system. The results showed that the radiation intensity I_0 changes around 5% near the edge of the detector, and only around 2% at the central region of the detector where the breast is imaged. The relatively small change in the radiation intensity is probably due to the fact that the PSD is placed close to the patient and the diameter of the pinhole (2 mm) is much larger than the focal spot size. For this reason, we did not perform any correction for the scatter measurement in this study. With that being said, the off-focal spot radiation correction is necessary and helpful for a more general purpose.[44,45]

Due to limited sampling points, the spatial interpolation might not be able to restore the structural variation of the scatter signal around object boundaries, leaving an irregular fluctuation in those regions. Local anatomy or metal implants will also create structural variation of scatter signal, which might not be sampled. To address this problem, correction is performed on the SPR map based on prior knowledge. In this study, we use a maximum SPR constraint for the correction. When computational time is not a concern, one can also utilize the scatter samples at the neighboring angular projections to restore the variations of scatter as proposed by Yan et al.[22] The data redundancy in the projection views might also be used to interpolate the scatter, reducing the number of projections acquired in the additional scan and therefore reducing the scanning time and patient dose.

The f-SPR scatter correction algorithm is implemented with MATLAB® and it is run on a customized workstation equipped with an Intel Core i7-5930K CPU. Currently, it takes 30 s to correct one projection image. When utilizing six cores and the MATLAB® parallel computing toolbox, the whole scatter correction can be completed in 1.5 min for s-DBT images or 2.5 min for the s-DCT images. The computational time could be further reduced by utilizing GPU hardware.

5 Conclusion

A new method, named f-SPR, for estimating scatter profile from a sparsely sampled primary signal is proposed. The f-SPR method combines the advantages of both the direct SI method, which enhances the contrast but fails to reduce noise, and ISPR method, which reduces the noise level but fails to improve the local contrast. With different levels of filtering, it balances between the SI and the ISPR scatter estimations. The f-SPR method is demonstrated using breast phantoms and PSD on an s-DBT system, and image quality in terms of CR, SDNR, and MTF was evaluated and compared with two direct interpolation methods. Significant improvement in image quality was observed using the f-SPR method compared to the direct interpolation methods with very small changes in

image resolution. Reconstruction of a human cadaver with f-SPR scatter correction showed a significantly improved CR and conspicuity while maintaining a similar noise level compared to that without scatter correction. The f-SPR method proposed in the paper may be used in any imaging systems where the scatter/primary signal can be sampled accurately. The application of the f-SPR scatter correction technique could lead to an improved image quality and reduction in radiation dose in x-ray imaging.

Disclosures

The content is solely the responsibility of the authors and does not necessarily represent the official views of the NIH. Otto Zhou has equity ownership and serves on the board of directors of Xintek, Inc., to which the technologies used or evaluated in this article have been or will be licensed. Jianping Lu has equity ownership in Xintek, Inc.

Acknowledgments

The authors would like to thank Yuan Lin and Tian Cao for helpful discussions on image processing. This work is partially supported by NCI-funded Carolina Center for Cancer Nanotechnology Excellence (5U54CA151652), a grant from the NCI (5R21CA185741), and The University of North Carolina School of Medicine Team Translation Science Award (TTSA001P2).

References

1. E.-P. Ruhrnschopf and K. Klingenbeck, "A general framework and review of scatter correction methods in x-ray cone-beam computerized tomography. Part 1: scatter compensation approaches," *Med. Phys.* **38**(7), 4296–4311 (2011).
2. E.-P. Ruhrnschopf and K. Klingenbeck, "A general framework and review of scatter correction methods in cone beam CT. Part 2: scatter estimation approaches," *Med. Phys.* **38**(9), 5186–5199 (2011).
3. H. Aichinger et al., *Radiation Exposure and Image Quality in X-Ray Diagnostic Radiology: Physical Principles and Clinical Applications*, Springer, Berlin (2012).
4. H. Aichinger et al., *Physical Principles and Clinical Applications: Radiation Exposure and Image Quality in X-Ray Diagnostic Radiology*, Springer, Berlin, Heidelberg (2012).
5. T. Patel, H. Peppard, and M. B. Williams, "Effects on image quality of a 2D antiscatter grid in x-ray digital breast tomosynthesis: initial experience using the dual modality (x-ray and molecular) breast tomosynthesis scanner," *Med. Phys.* **43**(4), 1720–1735 (2016).
6. W. Zbijewski and F. J. Beekman, "Efficient Monte Carlo based scatter artifact reduction in cone-beam micro-CT," *IEEE Trans. Med. Imaging* **25**(7), 817–827 (2006).
7. H. P. Chan and K. Doi, "The validity of Monte Carlo simulation in studies of scattered radiation in diagnostic radiology," *Phys. Med. Biol.* **28**(2), 109–129 (1983).
8. A. P. Colijn and F. J. Beekman, "Accelerated simulation of cone beam x-ray scatter projections," *IEEE Trans. Med. Imaging* **23**(5), 584–590 (2004).
9. A. Miceli et al., "Monte Carlo simulations of a high-resolution x-ray CT system for industrial applications," *Nucl. Instrum. Methods Phys. Res. Sect. A* **583**(2–3), 313–323 (2007).
10. Y. Kyriakou, T. Riedel, and W. A. Kalender, "Combining deterministic and Monte Carlo calculations for fast estimation of scatter intensities in CT," *Phys. Med. Biol.* **51**(18), 4567–4586 (2006).
11. A. Badal and A. Badano, "Accelerating Monte Carlo simulations of photon transport in a voxelized geometry using a massively parallel graphics processing unit," *Med. Phys.* **36**(11), 4878–4880 (2009).
12. K. Kim et al., "Fully iterative scatter corrected digital breast tomosynthesis using GPU-based fast Monte Carlo simulation and composition ratio update," *Med. Phys.* **42**(9), 5342–5355 (2015).
13. X. Jia et al., "A GPU tool for efficient, accurate, and realistic simulation of cone beam CT projections," *Med. Phys.* **39**(2012), 7368–7378 (2012).
14. R. Ning, X. Tang, and D. Conover, "X-ray scatter correction algorithm for cone beam CT imaging," *Med. Phys.* **31**(5), 1195–1202 (2004).
15. K. P. Maher and J. F. Malone, "Computerized scatter correction in diagnostic radiology," *Contemp. Phys.* **38**(2), 131–148 (1997).
16. K. Yang, G. Burkett, and J. M. Boone, "A breast-specific, negligible-dose scatter correction technique for dedicated cone-beam breast CT: a physics-based approach to improve Hounsfield unit accuracy," *Phys. Med. Biol.* **59**(21), 6487–6505 (2014).
17. I. Sechopoulos, "X-ray scatter correction method for dedicated breast computed tomography," *Med. Phys.* **39**(5), 2896–2903 (2012).
18. L. Zhu and L. Xing, "Measurement-based scatter correction for cone-beam CT in radiation therapy," *Proc. SPIE* **7258**, 72583C (2009).
19. T. Niu and L. Zhu, "Scatter correction for full-fan volumetric CT using a stationary beam blocker in a single full scan," *Med. Phys.* **38**(11), 6027–6038 (2011).
20. A. Peterzol, J. M. Létang, and D. Babot, "A beam stop based correction procedure for high spatial frequency scatter in industrial cone-beam x-ray CT," *Nucl. Instrum. Methods Phys. Res. Sect. B* **266**(18), 4042–4054 (2008).
21. J. S. Maltz et al., "Focused beam-stop array for the measurement of scatter in megavoltage portal and cone beam CT imaging," *Med. Phys.* **35**(6), 2452–2462 (2008).
22. H. Yan et al., "Projection correlation based view interpolation for cone beam CT: primary fluence restoration in scatter measurement with a moving beam stop array," *Phys. Med. Biol.* **55**(21), 6353–6375 (2010).
23. K. Schörner, M. Goldammer, and J. Stephan, "Comparison between beam-stop and beam-hole array scatter correction techniques for industrial x-ray cone-beam CT," *Nucl. Instrum. Methods Phys. Res. Sect. B* **269**(3), 292–299 (2011).
24. L. Zhu, N. R. Bennett, and R. Fahrig, "Scatter correction method for x-ray CT using primary modulation: theory and preliminary results," *IEEE Trans. Med. Imaging* **25**(12), 1573–1587 (2006).
25. L. Ritschl et al., "Robust primary modulation-based scatter estimation for cone-beam CT," *Med. Phys.* **42**(1), 469–478 (2015).
26. C. R. Inscoe et al., "Demonstration of a scatter correction technique in digital breast tomosynthesis," *Proc. SPIE* **8668**, 86680H (2013).
27. C. R. Inscoe et al., "Low dose scatter correction for digital chest tomosynthesis," *Proc. SPIE* **9412**, 941248 (2015).
28. Y. Kim et al., "An experimental study of practical computerized scatter correction methods for prototype digital breast tomosynthesis," *Proc. SPIE* **9033**, 903314 (2014).
29. R. Ning, X. Tang, and D. Conover, "X-ray scatter correction algorithm for cone beam CT imaging," *Med. Phys.* **31**(5), 1195–1202 (2004).
30. K. Yang, G. Burkett, Jr., and J. M. Boone, "An object-specific and dose-sparing scatter correction approach for a dedicated cone-beam breast CT system using a parallel-hole collimator," *Proc. SPIE* **8313**, 831303 (2012).
31. S. S. Jia Feng and I. Sechopoulos, "A software-based x-ray scatter correction method for breast tomosynthesis," *Med. Phys.* **38**(12), 6643–6653 (2011).
32. L. Zhu, J. Wang, and L. Xing, "Noise suppression in scatter correction for cone-beam CT," *Med. Phys.* **36**(3), 741–752 (2009).
33. J. Star-Lack et al., "Efficient scatter correction using asymmetric kernels," *Proc. SPIE* **7258**(12), 72581Z (2009).
34. N. Otsu, "A threshold selection method from gray-level histograms," *IEEE Trans. Syst., Man, Cybern.* **9**(1), 62–66 (1979).
35. D. Sandwell, "Biharmonic spline interpolation of GEOS-3 and SEASAT altimeter data," *Geophys. Res. Lett.* **14**(2), 139–142 (1987).
36. E. Samei et al., "Comparative scatter and dose performance of slot-scan and full-field digital chest radiography systems," *Radiology* **235**, 940–949 (2005).
37. I. Sechopoulos et al., "Scatter radiation in digital tomosynthesis of the breast," *Med. Phys.* **34**(2), 564–576 (2007).
38. J. Shan et al., "Stationary chest tomosynthesis using a carbon nanotube x-ray source array: a feasibility study," *Phys. Med. Biol.* **60**(1), 81–100 (2015).
39. X. Qian et al., "High resolution stationary digital breast tomosynthesis using distributed carbon nanotube x-ray source array," *Med. Phys.* **39**(4), 2090–2099 (2012).

40. G. Wu et al., "Adapted fan-beam volume reconstruction for stationary digital breast tomosynthesis," *Proc. SPIE* **9412**, 94123J (2015).
41. A. Andersen and A. Kak, "Simultaneous algebraic reconstruction technique (SART): a superior implementation of the ART algorithm," *Ultrasonic Imaging* **6**, 81–94 (1984).
42. H. Fujita et al., "A simple method for determining the modulation transfer function in digital radiography," *IEEE Trans. Med. Imaging* **11**(1), 34–39 (1992).
43. K. Pearson, "Note on regression and inheritance in the case of two parents," *Proc. R. Soc. London* **58**(58), 240–242 (1895).
44. X. Dong et al., "Relationship between x-ray illumination field size and flat field intensity and its impacts on x-ray imaging," *Med. Phys.* **39**(10), 5901–5909 (2012).
45. E. S. M. Ali and D. W. O. Rogers, "Quantifying the effect of off-focal radiation on the output of kilovoltage x-ray systems," *Med. Phys.* **35**(9), 4149–4160 (2008).

Biographies for the authors are not available.